1-4-2024

Experimental Environmental Profiles and Sloshing Dynamics Aboard Zero-G Aircraft

Pedro J. Llanos
Embry-Riddle Aeronautical University, llanosp@erau.edu

Sathya Gangadharan
Embry Riddle Aeronautical University, sathya@erau.edu

Kevin Crosby
Carthage College

10.2514/6.2024-0083

Experimental Environmental Profiles and Sloshing Dynamics Aboard Zero-G Aircraft

Pedro J. Llanos[1] and Sathya Gangadharan[2]
Embry-Riddle Aeronautical University, Daytona Beach, Florida, 32114, USA

Kevin Crosby[3]
Carthage College, Kenosha, Wisconsin, 53140, USA

This study presents the results of a parabolic flight experiment to study the sloshing dynamics of the magneto-active propellant management device experiment. This device utilizes a magneto-active membrane and magnets located external to the tank to effectively damp the liquid free surface motion. This research work establishes a benchmark with sloshing analytical formulation and sensor calibration methods that can be used to characterize future research parabolic flights while providing important environmental profiles measured during flight, such as accelerations, pitch angle, velocity, temperature, total volatile content, carbon dioxide, relative humidity, magnetic field, and radiation. Correlation between these flight variables and the sloshing experiment are suggested to improve suppression of sloshing. Preliminary postflight analysis suggests a close correlation between high peaks of carbon dioxide and total volatile compound levels during the parabolas – levels sustained for up to one hour combined during cruise in some parabolic flights.

I. Nomenclature

ERAU = Embry-Riddle Aeronautical University
ISS = International Space Station
MAPMD = Magneto Active Propellant Management Device
MASCS = Magneto-Active Slosh Control System
TRL = Technology Readiness Level
TVOC = Total volatile compound

II. Introduction

This research was conducted as part of a NASA Flight Opportunities program to support flown experiments aboard Zero-G aircraft when conducting eight parabolic flights. Embry-Riddle Aeronautical University (ERAU) and Carthage College jointly collaborated on this project. One of the purposes of this paper is to highlight important variables that can be used to better understand prospective experiments during parabolic flights, leverage the efforts of data interpretation, and test and validate some of the avionics hardware and software that can be used for prospective parabolic and suborbital flights.

Previous work has been conducted to characterize some of the environment and dynamics of parabolic flights [1], [2]. Our work entails a more comprehensive and detailed characterization to help other researchers with their research activities of related flight operations, flight dynamics and aircraft environment characteristics when conducting parabolic flights. Relevant data for each flight is provided, such as in-flight acceleration recordings using various sensors, temperature and relative humidity profiles, intensity of the magnetic field (north, vertical, and horizontal),

[1] Associate Professor in Space Operations, Applied Aviation Sciences, AIAA Senior Member.
[2] Professor in Mechanical Engineering, Mechanical Engineering Department. AIAA Associate Fellow.
[3] Professor in Physics and Astronomy Department and Computer Science Department, AIAA Senior Member.

carbon dioxide, total volatile contents, radiation levels, and other aerodynamic attitude variables such as pitch (most relevant to parabolas), yaw and roll during each parabolic flight.

Our suite of sensors was essential to support the main experiment of parabolic flight, the magneto-active propellant management device (MAPMD). This experiment has made significant technological progress [3], and we hope to continue maturing the technology readiness level (TRL) of such device. The MAPMD is a free-floating (under gravity) diaphragm positioned within the liquid using small magnetic field gradients applied by external magnets. When subject to surface waves or low-gravity slosh, the displacement of the membrane is countered by the external magnetic field and the incipient slosh is damped. The objective of this effort is to demonstrate the feasibility of using MAPMD to reduce destabilizing liquid slosh during vehicle maneuvers, increasing mission safety and reducing costs. This would benefit NASA missions, the commercial space industry, and other government agencies.

Our Science, Technology, Engineering and Math (STEM) experiments allowed students to gain hands-on experimental design and test these technologies in reduced gravity conditions (e.g., weightlessness, Lunar, and Mars gravity). Parabolic flights are also used as a spaceflight analog to conduct short-period parabolas and assess the effects of weightlessness on the human physiology [4].

Parabolic flights are thought to have a considerable impact on the attentional load when conducting parabolic experiments [5]. Besides the International Space Station (ISS) and the Chinese station, parabolic flights are considered the only platform to mimic weightlessness and conduct human-operated experiments in flight [6]. Suborbital flights can also support these experiments but with no direct human interaction. As NASA's Flight Opportunities program continues to spark interest in STEM careers [7], and suborbital technologies continue advancing, soon we will witness the first space flight participants flying aboard suborbital vehicles that will operate short suborbital research activities.

A. Operations

Flight operations were conducted on two flight campaigns, November 13, 15, 16, 17, 2019 from Sandford International airport (SFB), and November 17, 18, 19, 21, 2020 from Fort Lauderdale airport (FLL) onboard a Boeing 727-200F modified aircraft (G-Force One®, Zero Gravity Corporation). Six sets of parabolas were performed with 5 parabolas per set each day in the first campaign, and 5, 5, 6, 5 parabolas per set in the second campaign. The total number of parabolas was 120 and 121 in the first and second campaign, respectively. Various types of microgravity parabolas were targeted, Mars G, Lunar G, and 0 G. These parabolas are identified in each flight.

B. Dynamics of Flight

Understanding the dynamics of the flight is crucial to aid us in the interpretation of data.

Fig. 1a shows a schematic of what a parabola looks like. Although theoretically speaking, we refer to parabolic flight, we will see in our analysis that this is not quite a parabola but rather a quasi-parabola. The aircraft transitions from 1 g at cruise to hypergravity (1.8g) for about 20 seconds before entering the microgravity phase (0g) for about 25 seconds, then transitions again to a second hypergravity phase (1.8g).

Fig. 1b depicts the forces acting on the aircraft when the aircraft is performing a parabola with respect to the coordinate axis shown in the figure.

Fig. 1c displays the location of the NanoLab (A NanoLab has the size of a two-form factor of a cube shaped unit or CubeSat, 10 cm x 10 cm x 20 cm) and the edl-XYZ data logger. The x-direction points from the tail to front of the aircraft, the y-direction points from left to right wings, and the z-direction points from the floor to the ceiling similar as it was done it previous studies [5].

Fig. 1d shows the interior of the NanoLab with the suit of individual sensors.

C. Sensor Suite

Our suite of sensors was flown during 180 parabolas in weightlessness, Martian and Lunar gravities combined in several flights in 2019 and 2020, and such technologies were also flown in 2021 to cross validate prior flight collected data. In-flight data was conducted using state-of-the-art sensors: MPU9250 accelerometer, gyro sensor, and magnetometer sensor, the SI7021 temperature and humidity sensor, the LIS331 (ultra-low-power high performance three axes linear accelerometer), an air quality sensor or metal oxide sensor (CO_2, total volatile content), the HMCL5883L triple axis magnetometer sensor, and the pocket Geiger radiation sensor. All these sensors were obtained from SparkFun Electronics. In addition to these sensors, the edl-XYZ multi-use data logger also flown in a suborbital flight aboard Blue Origin's New Shepard [8], was used to measure acceleration, temperature, and relative humidity. Redundant sensors were used for comparison and data validation. The mathematical formulation for the calibration of the suite of sensors is provided in Section IV, including calibration of the acceleration, pitch angle (using acceleration data, quaternions, and filter), magnetic field and velocity profiles of the aircraft.

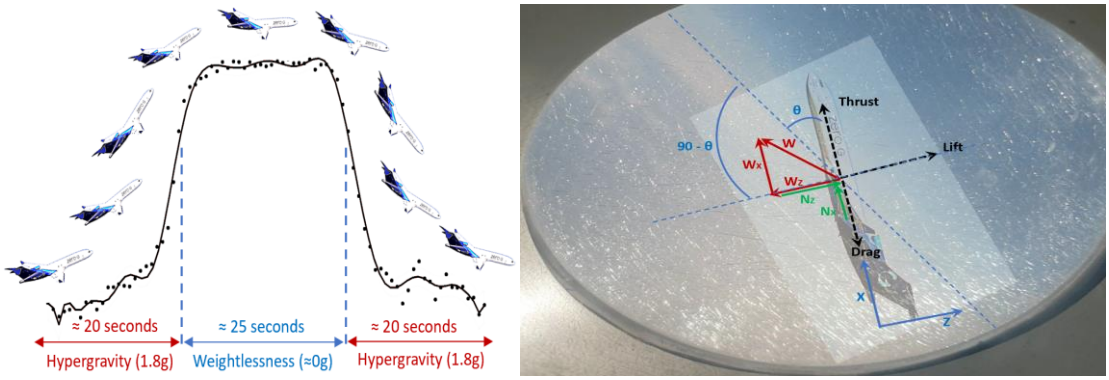

(a) (b)

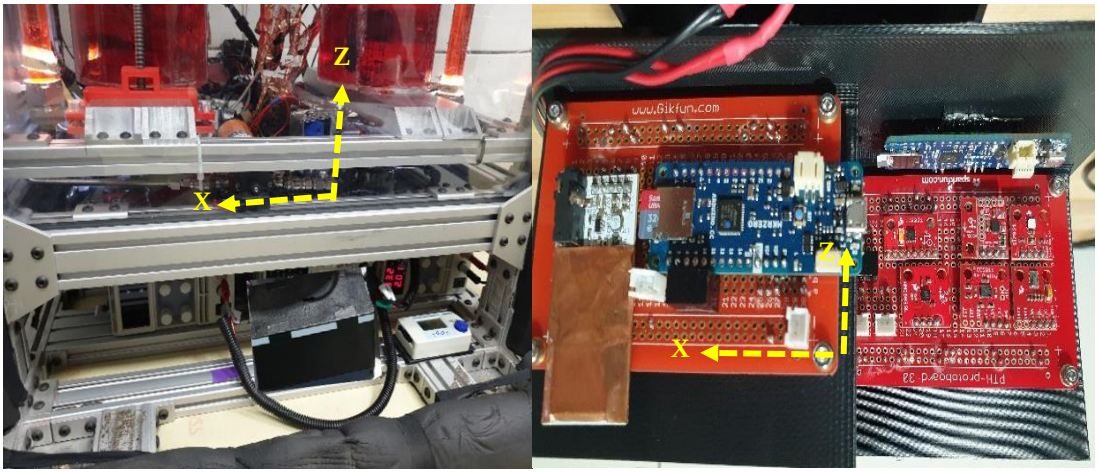

(c) (d)

Fig. 1 Parabolic flight dynamics and experimental set up. a) Schematics of parabola. b) Forces acting on aircraft. c) NanoLab and edl-XYZ data logger. d) Interior of NanoLab showing suit of sensors. Yellow coordinates show the x-direction (thrust travel) and the z-direction (lift direction)

III. Methodology

A. Flight Campaign 2020

Fig. 2 depicts the parabolic flights for the 2020 flight campaign and an example of an acceleration profile for one of the flights.

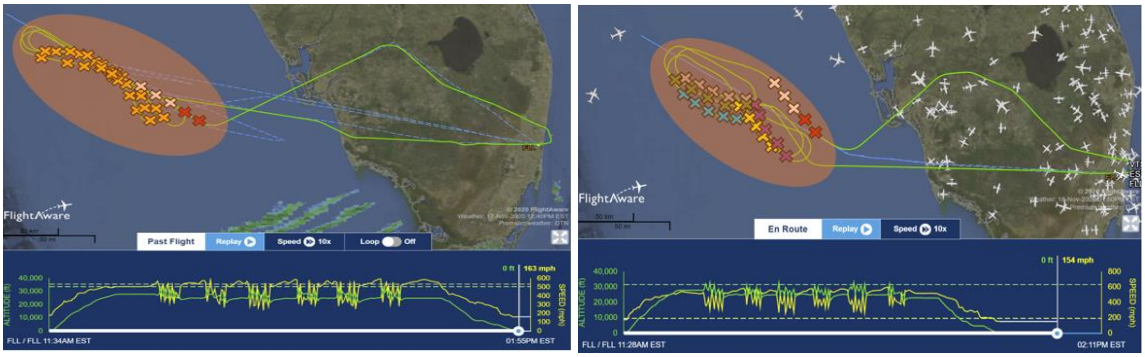

a) b)

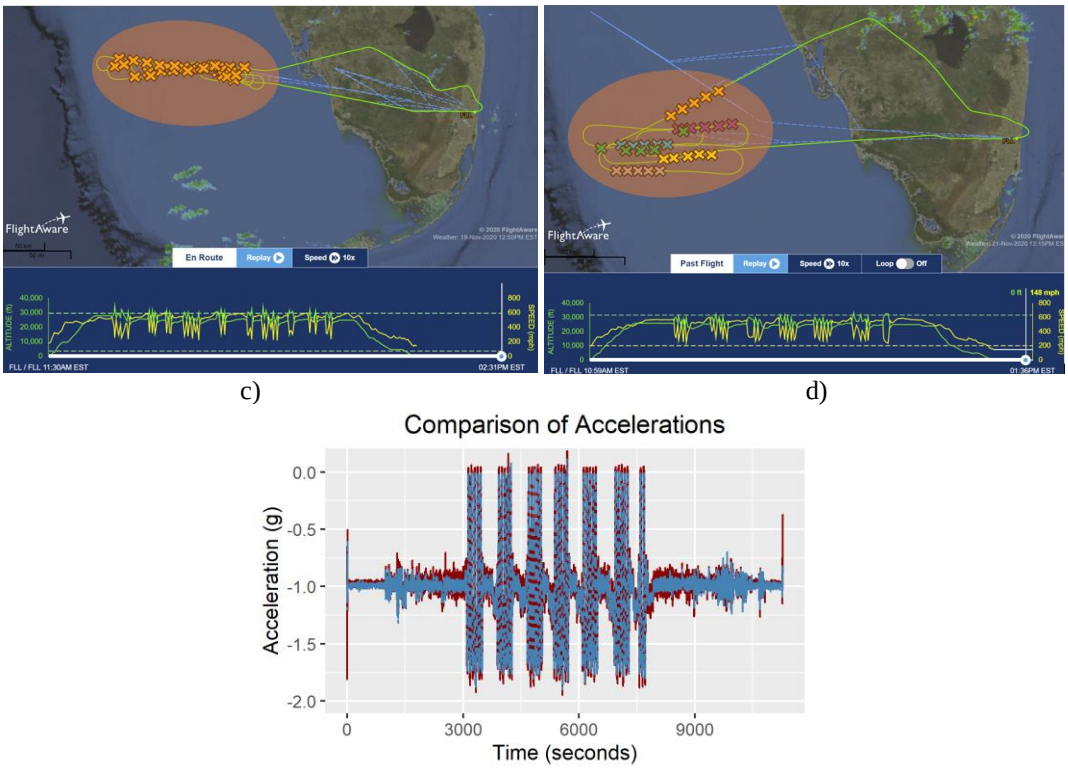

Fig. 2 Parabolic flights November 17, 18, 19, 21 of 2020. e) Comparison of acceleration profile for the Nov 19 parabolic flight with two different sensors

Fig. 3 displays several flight parabolas showing a Martian parabola, a Lunar parabola and two microgravity parabolas. The y-axis corresponds to the normal acceleration for each of the parabolas. The x-axis is the time of the parabola measured by the suite of sensors.

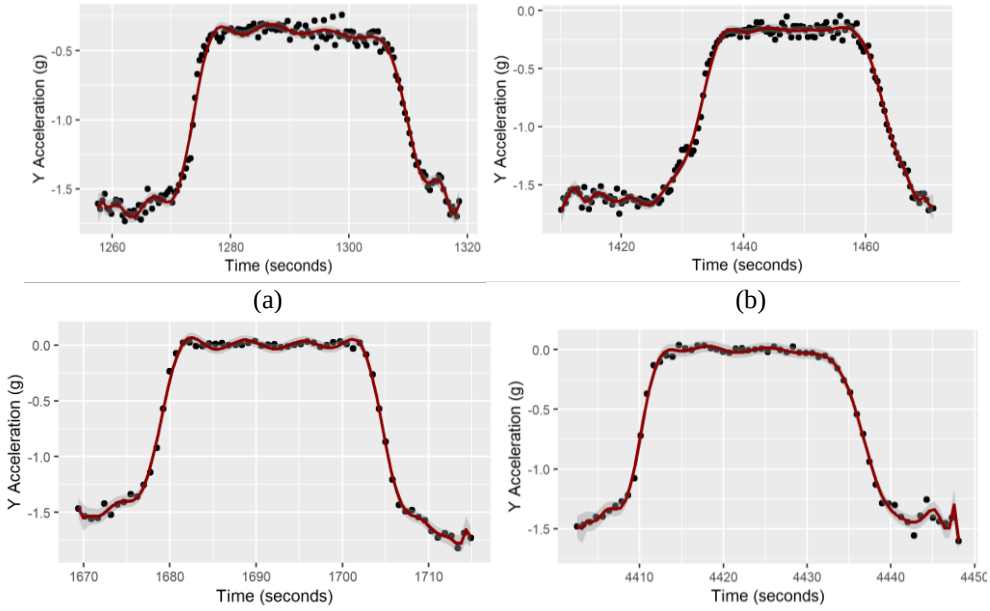

Fig. 3 Example of parabolic flights flown on November 17th, 2020: a) Mars parabola. b) Lunar parabola. Example of microgravity parabolas flown on November 19th, 2020: : c) Parabola 7th. d) Parabola 22nd.

Rstudio software and Excel were used to process and analyze all the parabolic data.

B. Magneto Active Propellant Management Device (MAPMD)

The MAPMD rig shown in Fig. 4. The dimensions of the tank are 18 inches in height by 6 inches in diameter. In our simulations, the diameter of the membrane is approximately 6 inches or about 15 cm.

Fig. 4 MAPMD rig.

Fig. 5a and Fig. 5b shows the amplitudes generated during microgravity by each parabola and the corresponding maximum amplitude achieved for each parabola, respectively. The amplitudes were obtained from the recorded videos in flight. This is the first step towards computing the force of the fluid on the membrane and tank.

The motion of the ferromagnetic membrane and liquid during flight will be described too. From the recorded videos in flight, the researchers extracted the approximated tilt of the membrane at each time stamp for each of the parabolas. Results of the membrane dynamics are presented in the results section.

IV. Results

Redundant sensors were used for comparison and data validation for post-data flight analysis. Preliminary data analysis shows that the calibration of the post-flight acceleration data was within 6% error when comparing several accelerometers data using different sensors. This difference was consistent during different parabolas.

Carbon dioxide levels average values measured ranged between 400 ppm to about 1000 ppm with maximum values between 1500 ppm to 4000 ppm during several segments of the parabolic flight. The average total volatile content measured was around 1.5 mg/m3 to near 10 mg/m3 with maximum values found in the range of about 100 mg/m3 to about 5000 mg/m3. There is a correlation between high peaks of carbon dioxide and total volatile content levels that are sustained for up to one hour combined during cruise in some parabolic flights. Calibration of the magnetic field, aircraft velocity and pitch angle were also obtained for each of the parabolic flights.

Preliminary analysis [9] of the forces on the cylindrical tank wall have been found to be as high as 60 N during microgravity phase and between -40N to +40N during the hypergravity phases (ascent and descent) for a few milliseconds (parabola 22nd for the November 19 2020 flight campaign, see Fig. 2e). Such large forces are due to the translation motion of the ferromagnetic membrane inside the tank.

A longer duration microgravity time through a suborbital flight test is recommended and currently being pursued as a payload experiment in PLD Space's MIURA I suborbital rocket. For the upcoming suborbital flight, evaluation of crucial flow parameters such as pressure, water level, membrane and liquid distribution 3D capture, and liquid forces on the tank during the flight mission are recommended.

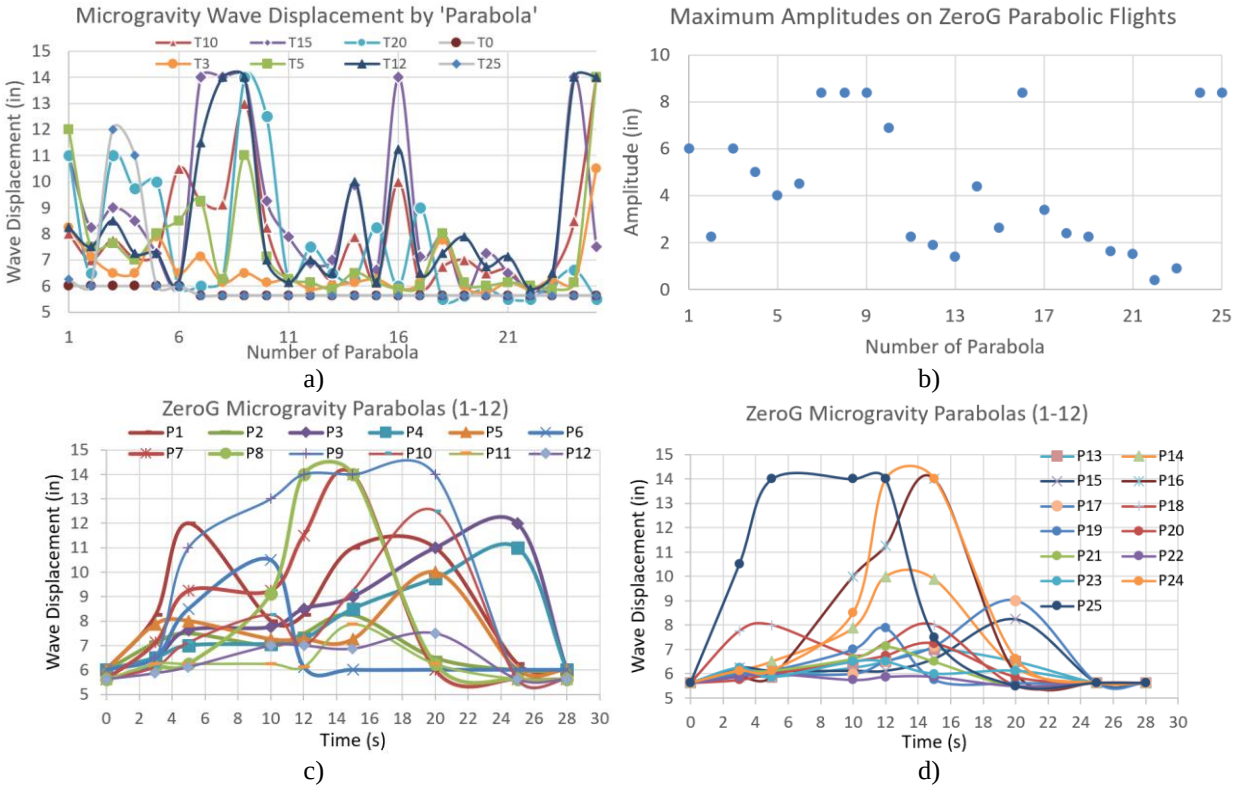

Fig. 5 Amplitudes for each parabola during microgravity. a) microgravity amplitudes by number of parabolas. b) Maximum amplitude for each parabola. c) Microgravity parabolas 1-12. d) Microgravity parabolas 13-25.

Fig. 5b-c shows 9-time segments: T1 (0 seconds), T2 (3 seconds), T3 (5 seconds), T4 (10 seconds), T5 (12 seconds), T6 (15 seconds), T7 (20 seconds), T8 (25 seconds), and T9 (28 seconds). From Fig. 5b and Fig. 5c we can extract several observations about the equilibration time [10] of the liquid in microgravity. In their study, they provide that the predicted time in which the liquid can be started in microgravity is given by Eq. (1):

$$t_s = 0.4 \cdot \sqrt{\frac{\rho {R_t}^3}{\sigma}} \tag{1}$$

From our collected data (Fig. 7), we can see that most parabolas have two maxima in time. The first local maximum occurs at about 5 seconds which corresponds to the time obtained using a variation of Eq. (2):

$$t_s = 0.75 \cdot \sqrt{\frac{\rho {R_t}^3}{\sigma}} \tag{2}$$

The second local maximum occurs between 15 (for most parabolas) to 20 seconds and is obtained using an averaged estimated time given by Eq. (3):

$$t_s = 2.5 \cdot \sqrt{\frac{\rho {R_t}^3}{\sigma}} \tag{3}$$

where ρ is the liquid density (in our case we assumed water to have a density of 1000 kg/m3), R_t is the radius of the tank, and σ is the surface tension of the liquid (for water is 0.072 N/m at room temperature). In Fig. 6a, we show the results for a cylindrical tank filled with water at 33% with the input parameters displayed in Fig. 6. The SWRI software tool is used to compute the parameters of a mechanical pendulum analog to the fluid dynamics of a sloshing in a cylindrical tank. The tank is defined as four straight segments (units in meters) defined by the end coordinates of the

radial distance (R) and height (Z): a horizontal flat bottom (segment 1), a horizontal top (segment 3) and two vertical straight segments (segments 2 and 4) representing the cylindrical walls. The height of the cylinder is 0.45m and the radius of the cylinder is 0.15m. We used g= 0.01 m/s2 as an average microgravity that was recorded for most of the parabolas. The software outputs the computed mechanical pendulum model parameters.

Rmax (m)	0.15	
Zmax (m)	0.45	
Nsegs	4	
Segment 1 Type	REnd=0.15	Zend= 0
Segment 2 Type	REnd=0.15	Zend=0.45
Segment 3 Type	REnd=0	Zend=0.45
Segment 4 Type	REnd=0	Zend=0
Liq.Ht	0.15	
Density (kg/m^3)	1000	
Kin.Viscosity (m^2/s)	0.000001	
Gravity (m/s^2)	0.01	

LIQUID MASS [mass units]	10.60288
LIQUID SURFACE HEIGHT above z=0 [length units]	0.15
FIRST MODE PARAMETERS	
Pendulum mass [mass units]	4.622091
Pendulum length [length units]	0.084942
Pendulum hinge z-location [length units]	0.118702
Pendulum % critical damping	1.10594
Ratio of slosh amplitude to pendulum amplitude	1.477778
SECOND MODE PARAMETERS	
Pendulum mass [mass units]	0.145031
Pendulum length [length units]	0.028136
Pendulum hinge z-location [length units]	0.122761
Pendulum % critical damping	1.10594
Ratio of slosh amplitude to pendulum amplitude	0.388801
FIXED MASS PARAMETERS	
Mass [mass units]	5.835753
Z-location [length units]	0.107175
Mom. Inertia [mass*length^2 units]	0.065563

a) b)

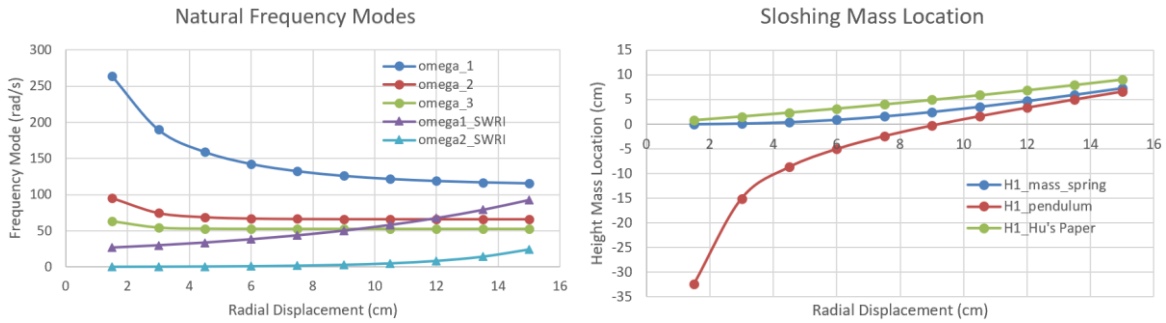

c) d)

Fig. 6 a) SLOSHXL Graphical User Interface Inputs. b) Outputs. c) First and second modes using the cylindrical tank damping model (SWRI) and the analytical form using Eq. (5). d) Estimated sloshing mass location using Eq. (6) for the first mode.

The analytical natural frequencies are obtained using Eq. (4) described in previous studies [11].

$$f_n = \frac{1}{2\pi}\sqrt{\frac{g\xi_n}{R}\tanh\left(\frac{\xi_n h}{R}\right)} \tag{4}$$

The first five natural frequencies, ω_n ($n \leq 5$) for the main sloshing modes [12] with nonzero lateral net force acting on the cylindrical tank wall can be written as in Eq. (5):

$$\omega_n = \sqrt{\frac{g\xi_n}{R}\tanh\left(\frac{\xi_n h}{R}\right)} \tag{5}$$

where ξ_1=1.841, ξ_2=5.331, ξ_3=8.536, ξ_4=11.706 and ξ_5=14.864 are the five roots of the derivatives of the Bessel function of the first kind given by $J_m(x_n) = \sum_{k=0}^{\infty} \frac{(-1)^k (x_n/2)^{m+2k}}{k!(m+k)!}$ for m=1. The derivative of the Bessel function of the first kind is given by: $J_1'(x_n) = \sum_{k=0}^{\infty} \frac{(-1)^k}{k!(1+k)!} \frac{(1+2k)}{2} (x_n/2)^{2k}$ where n =1, 2, 3 so that : $J_1'(x_1) = 1.841$, $J_1'(x_2) = 5.331$, and $J_1'(x_3) = 8.536$ are the first three roots of the derivatives of the Bessel function of first kind. The differential equation of the Bessel function can be expressed as $x^2y''(x) + xy'(x) + (x^2 - m^2)y = 0$ where the general solution can be approximated as $y = AJ_m(x)$ where is A is an arbitrary constant.

Note that the microgravity average value for most parabolas is about 0.01 m/s2 (value chosen in our simulations), thus the frequencies are not zero.

The sloshing mass location [12] or maximum displacement for each mode can also be estimated using formulation in Eq. (6) for a spring mass analog and pendulum analog, respectively :

$$\begin{aligned} \mathrm{H}_n &= \mathrm{h} - \frac{R}{\xi_n} \tanh\left(\frac{\xi_n h}{R}\right) \\ \mathrm{H}_n &= \mathrm{h} - \frac{R}{\xi_n}\left(\coth\left(\frac{\xi_n h}{R}\right) - \frac{1}{2}\operatorname{csch}\left(\frac{2\xi_n h}{R}\right)\right) \\ \mathrm{H}_n &= \mathrm{h} - \frac{R}{\xi_n}\left(\coth\left(\frac{\xi_n h}{R}\right) - \operatorname{csch}\left(\frac{\xi_n h}{R}\right)\right) \end{aligned} \tag{6}$$

The analytical natural frequency modes are displayed in Fig. 6b. The first sloshing mode is displayed in Fig. 6c. The second mode was not displayed since beyond a radial displacement of 10 cm, the frequencies are almost identical with less than 0.5% difference.

A similar analysis (like in Fig. 6 for microgravity parabolas) for the Martian (g=3.71 m/s2) and Lunar (g=1.62 m/s2) parabolas can be obtained using the same approach.

Fig. 7 depicts a first approximation of the water displacement when being sloshed during a microgravity. Fluid does not show as a steady-state behavior late in the first hypergravity phases (start of microgravity) or early in the second hypergravity phase (end of microgravity phase). Both membrane and fluid have a more chaotic downward motion during the second hypergravity phase as the microgravity phase is ending. Note that this data (Fig. 7a-b) corresponds to the control tank (not actively controlled) while the experimental tank (actively controlled) was forced to be still with a ring of magnets due to the inefficient magnetic force produced.

Although more data points may be needed to have more conclusive results, the first observation reveals that a more spread amplitude displacement takes place around 12 seconds of each parabola than at 5 seconds. At five seconds, the rate of displacement for parabolas 1-12 is between 3 in/s and 6 in/s and for parabolas 13-25 is between 3 in/s and 7 in/s although 10 out of the 12 parabolas show very close rate displacements about 3 in/s. Note that the rate of displacement at twelve seconds is between 3 in/s and 7 in/s for all 13-15 parabolas, with similar dispersions that for parabolas 1-12.

The natural frequencies during microgravity (level 0.01 m/s2) range from about 3.3% at 2.5cm from the center of the fluid to about 5.4% at the edge of the cylinder (15cm), the natural frequencies encountered during the Lunar (1.62 m/s2) and Mars (3.71 m/s2) parabolic flights ranged from about 0.4 to 0.7, and from about 0.6 to 1.0 within the same radial distances, respectively.

Fig. 7c displays the motion of the membrane during parabolic flight for each of the 25 parabolas at each time stamp (including an additional time step at T7 or seven seconds) as previously discussed. To assess the motion of the membrane of each parabola we would need to obtain the attitude of the aircraft (mainly pitch) which changes slightly for each microgravity parabola. We can obtain an approximate correlation of the cumulative motion of the membrane at each time step. The maximum relative motion of the membrane occurs when the velocity of water is near around 15 seconds, then at 20 seconds (13% less than at 15 seconds), then at 10 seconds (24% less than at 15 seconds), then at 5 seconds (52% less than at 15 seconds) and finally at 25 seconds (72% less than at 15 seconds). However, the cumulative velocity of water due to sloshing was recorded higher at 12 seconds, then at 5, 15, 7, 28, 10, 25 and 10 seconds, respectively. A clearer behavior understanding of the relative membrane motion and corresponding fluid velocity due to sloshing could be achieved with a further insight of the attitude and velocity of the aircraft, and a tighter time step size sample data collection., but we are leaving this for further research.

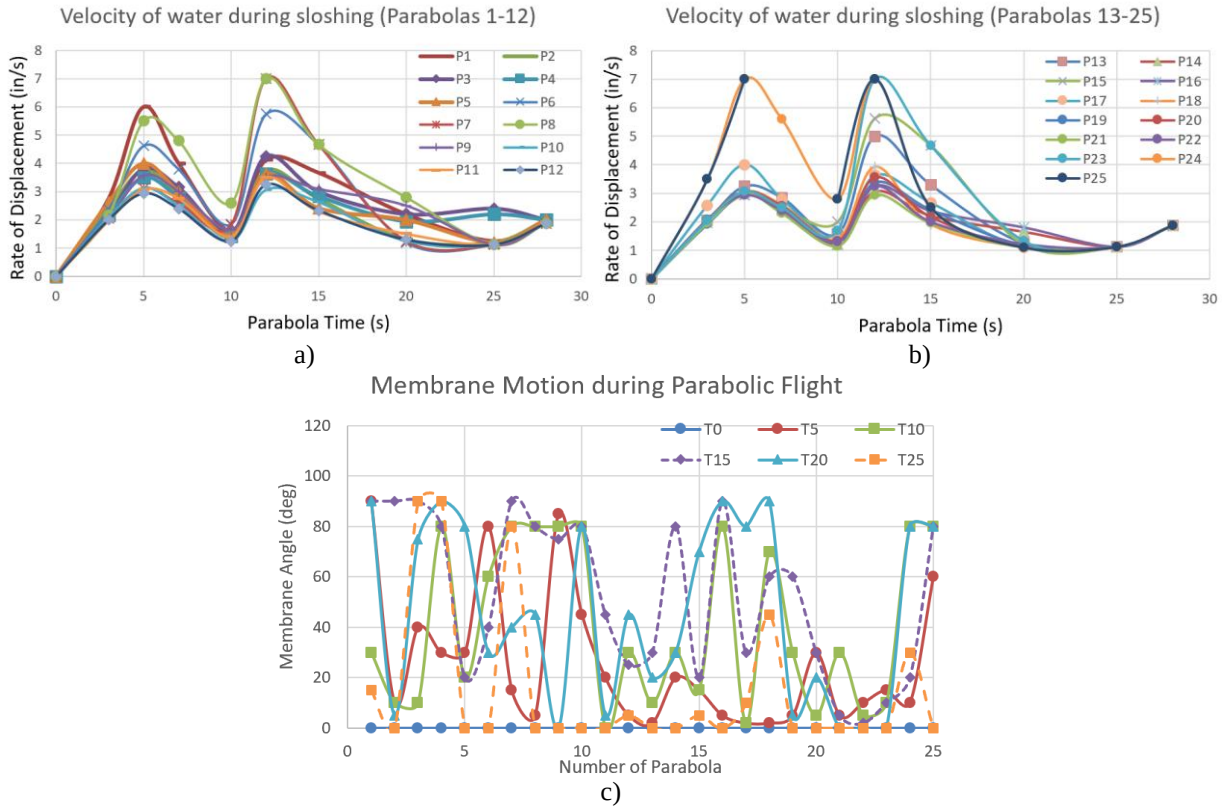

Fig. 7 a) Water displacement during microgravity for parabolas 1-12. b) Water displacement during microgravity for parabolas (13-25). c) Motion of membrane during flight. The legend symbols are T0 (0 seconds), T5 (5 seconds), T10 (10 seconds), T15 (15 seconds), T20 (20 seconds), T25 (25 seconds).

An example of the force on the tank wall during maximum amplitude wave for parabola 7th and parabola 22nd (Fig. 2e) can be obtained [13] as follows:

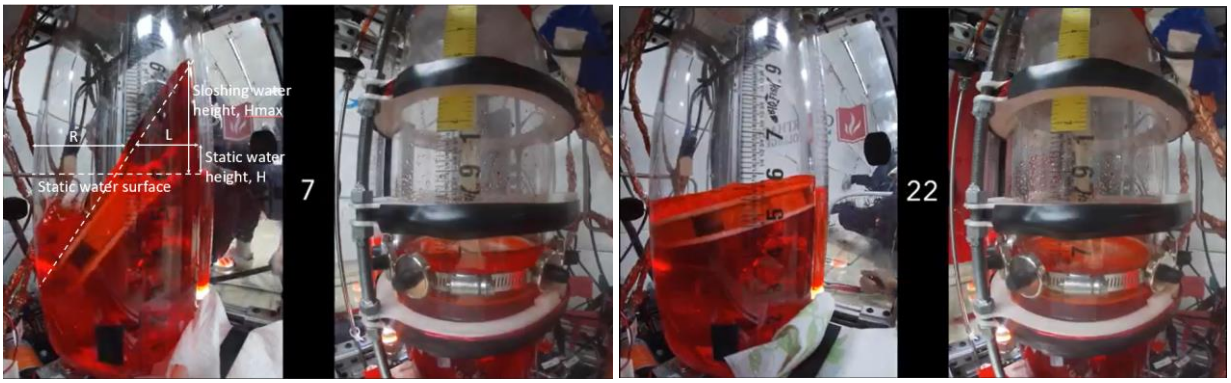

Fig. 8 Schematics of sloshing.

The pressure of water on the impact area (Fig. 8) of the wall for parabola 7 can be approximated by Eq. (7):

$$P = \rho g(H_{max} - H) = 1000\ kg/m^3 \cdot 0.01\ m/s^2 \cdot (3.25 - 0.75)in \cdot 2.54 \cdot 0.01 = 0.635\ Pa \qquad (7)$$

and the estimated impact area can be calculated as in Eq. (8):

$$L = R\frac{H_{max}-H}{H_{max}} = 6in \cdot \frac{3.25-0.75}{3.25} = 11.00\ cm = 0.11\ m \quad (8)$$

Thus, the estimated force is 0.635 Pa times the impact area or about 0.06979 N = 69.8 mN. Similarly, the force on the tank wall is 6.35 mN for parabola 22 (gravity = 0.005 m/s2), which is consistent with the force levels found in the CFD analysis performed using STAR-CCM+ in our previous study [9]. Here we showed two scenarios for large and small sloshing. The forces for any of the other parabolas fall within the range of these two scenarios.

A previous study [14] reveals that the equilibration time for the liquid in microgravity is typically on the order of 20-30 seconds. Note that this range corresponds for a suborbital flight with more steady state microgravity times (3.5 minutes of continuous microgravity) whereas our results show a typical equilibrium time for the liquid in microgravity between 15-20 seconds for 23 parabolas out of the 25 parabolas during a parabolic flight (discontinued microgravity). The sloshing frequencies for each parabola (Fig. 9) can be obtained using the displacement, x, formula $x=A\sin(\omega t)$ where A is the maximum amplitude, t is the time stamp and ω is the experimental frequency mode. For example, we can observe that the maximum frequency encountered was 0.79 rad/s during eight of the 25 parabolas, 0.52 rad/s during ten of the 25 parabolas, whilst most of the frequencies range between 0.31 rad/s and near 0.01 rad/s for the rest of the parabolas.

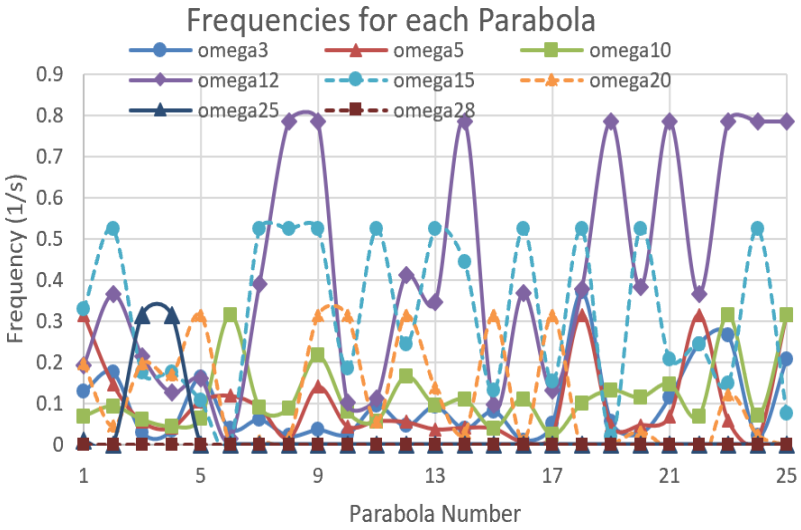

Fig. 9 Frequencies for each of the 25 parabolas.

The above study was conducted for the microgravity parabolas and a similar approach can be followed to analyze the Martian and Lunar parabolas. In our experiment, a fixed magnet was needed at the bottom of the tank since the suppression force was not sufficient to control the sloshing. A new proposed new configuration capable of generating one order of magnitude higher force is suggested to damp or suppress sloshing during microgravity conditions and this will be discussed next.

During our previous parabolic fight experiments, a remnant slosh suppression was observed, and the effective slosh damping did not meet our expectations. Our team is currently redesigning the magnetic membrane with multiple layers of a buoyant, ultrahigh-permeability metallic glass film to develop an optimized configuration of four current-carrying coils to increase magnetic force and field performance. Our upgraded MAPMD system (Fig. 10) Technology Readiness Level (TRL) is expected to be raised from 3 to 4 before our next microgravity flight campaigns. The system consists of a series of four Helmholt coils separated by a distance R, which is the radius of the transparent polycarbonate cylinder. A free-floating ferromagnetic membrane, made of multiple layers of a buoyant and ultrahigh-permeability metallic glass film, floats atop a fluid.

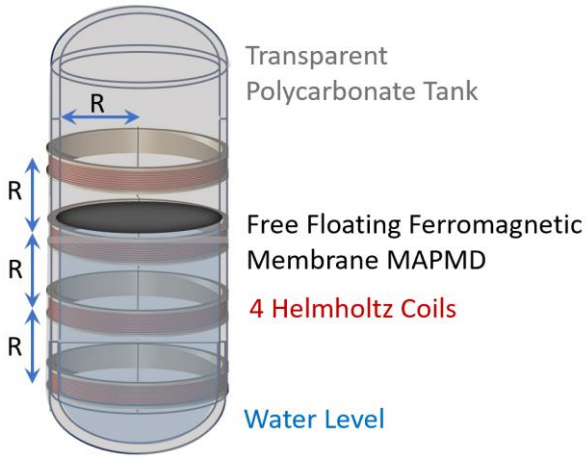

Fig. 10 Schematics of novel MAPMD.

This tank configuration has a similar shape as the cylindrical with domed top and bottom tank in the prospective mission to Europa Clipper set to launch in 2024 and the previous Cassini spacecraft.

A. Total Volatile Compounds and Carbon Dioxide Profiles

Next, we analyze the total volatile compounds (TVOC) during each parabolic flight in 2020. According to the World Health Organization (WHO), the total volatile compound is defined as the sum of all gases from the relevant organic compounds found in indoor air, also an indication of hygiene and indoor air quality (IAQ) (Meyer et al., 2021). Meyer's work [15] shows that a TVOC (<0.3 mg/m3) means the air quality is very good and not action is required (level 1). When TVOC is 0.3-1.0 mg/m3, the air quality is good, but ventilation is recommended (level 2). When TVOC is 1.0-3.0 mg/m3, the air quality is medium, ventilation is required and sourced would need to be identified (level 3). When TVOC is 3.0-10.0 mg/m3, the air quality is poor, and an increase of the ventilation is needed to refresh the air (level 4). When TVOC >10 mg/m3, the air quality is bad, and exposure should be limited for short periods (level 5). Carbon dioxide can be an indoor pollutant, highly toxic, colorless, and odorless, and a measure of ventilation effectiveness. It is suggested that a maximum of 1000 ppm CO2 is accepted for the indoor environment.

The CO2 (red) and total volatile compound (blue) were recorded aboard several parabolic flights. The CO2 levels are expressed in particles per million and the TVOC are expressed in particles per billion. We will talk more about the relevance of these results and extract several observations.

Based on the gathered data, during the first flight shows an average TVOC = 7.9 mg/m3 (1 mg/m3 is 1 ppb) excluding the last portion of the recorded flight which had a maximum TVOC = 325 mg/m3. This average TVOC would fall to level 4 according to the previous definition with poor air quality. The average CO2 level was 525.5 ppm, and the maximum CO2 was 1686 ppm.

In the second flight the average of the TVOC was 1.5 mg/m3 (level 3-medium air quality), with a maximum recorded value of 39 mg/m3. There are small spikes that correlate with each set of parabolas the aircraft conducted. The average CO2 level was 411.5 ppm and the maximum CO2 recorded was 659 ppm.

The third flight recorded an average TVOC value of 431 mg/m3 (level 5-bad air quality). There were three big spikes (Fig. 11) of extremely high TVOC values ~2600 mg/m3, ~3600 mg/m3 and 5065 mg/m3). Neglecting these spikes, the average TVOC for the first half of the flight was about 9.5 mg/m3 (level 3- poor air quality). The average CO2 level during flight was 959 ppm <1000 ppm (including the three peaks), and the maximum CO2 recorded was 4028 ppm. Note that these three peaks happened during the second segment of the flight where parabolas took place, and the average CO2 level during the first part of the flight was only ~ 75 ppm.

During the last flight of the 2020 campaign, the average of the TVOC was 129 mg/m3 (level 5-bad air quality). Excluding the two significant peaks (1290 mg/m3, 2774 mg/m3), the average TVOC is 5.6 mg/m3 (level 3-poor air quality). The average CO2 level was 710 ppm (including the two peaks) with a maximum value of 2965 ppm (level 5-bad air quality). The last two flights were part of the 2021 campaign for which the average TVOC was 2.94 mg/m3 (level 3-medium air quality) and 6.14 mg/m3 (level 4-poor air quality), respectively, and their maximum respective values of 74 mg/m3 and 64 mg/m3. The average CO2 levels were around 422 ppm and 442 ppm, respectively, and their associated maximum values were 889 ppm and 821 ppm. Individuals have different threshold tolerances to CO2 and TVOC levels so flight symptoms may vary depending on the concentrations at which everyone is exposed to.

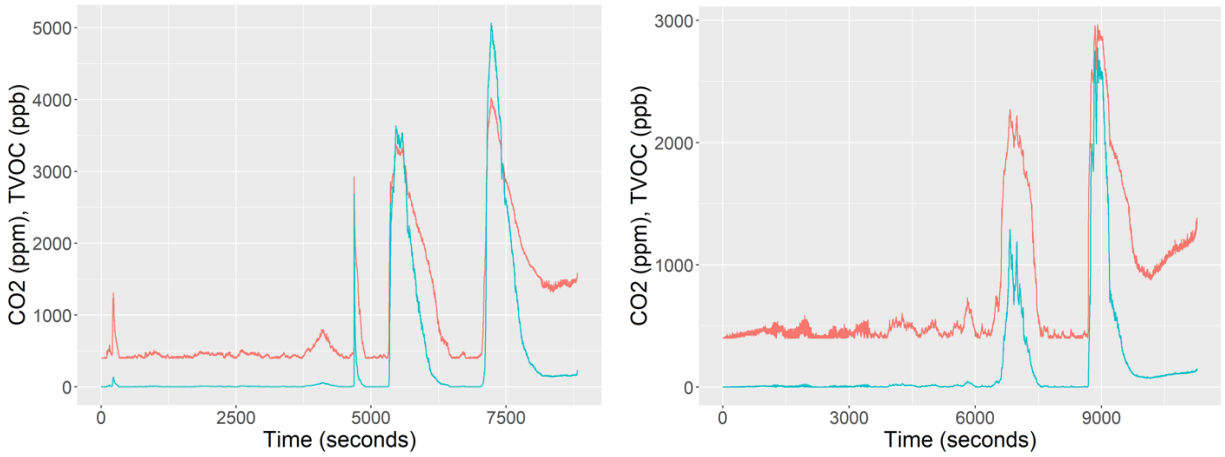

Fig. 11 CO2 and TVOC levels

The radiation levels encountered during all the flights ranged from about 0.2 to 0.33 mSv/h or about 1mSv per flight given that each flight was about 3-4 hours long on average. This is less than 10 mSV before any observable health effects may occur.

B. Pitch Angle Calibration Profiles

This section discusses the calibration of the pitch angle. The pitch angle, θ, was obtained using the quaternions during flight as in Eq. (9):

$$\theta = \arcsin\left(2 \cdot (-q_1 \cdot q_3 + q_0 \cdot q_2) \cdot \frac{180}{\pi} \cdot \mathrm{k}\right) \tag{9}$$

where q_0 is the scalar part and q_1, q_2, and q_3 are the components of the quaternion, k is filter parameter between 0 and 1. Thus, to calibrate the pitch angle, we needed to multiply the above equation by this filter parameter of 0.65 and 0.77 to get the pitch profiles in Fig. 12a below for both flights (Nov 17-18), respectively. For Fig. 12b (Nov 19 and 21), the filter parameter is 0.70 and 0.65 for both flights, respectively.

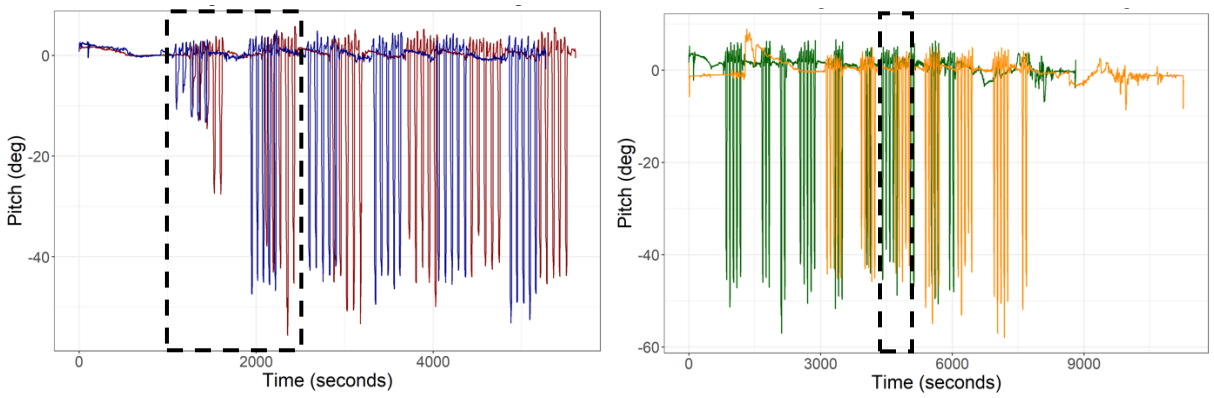

(a) (b)

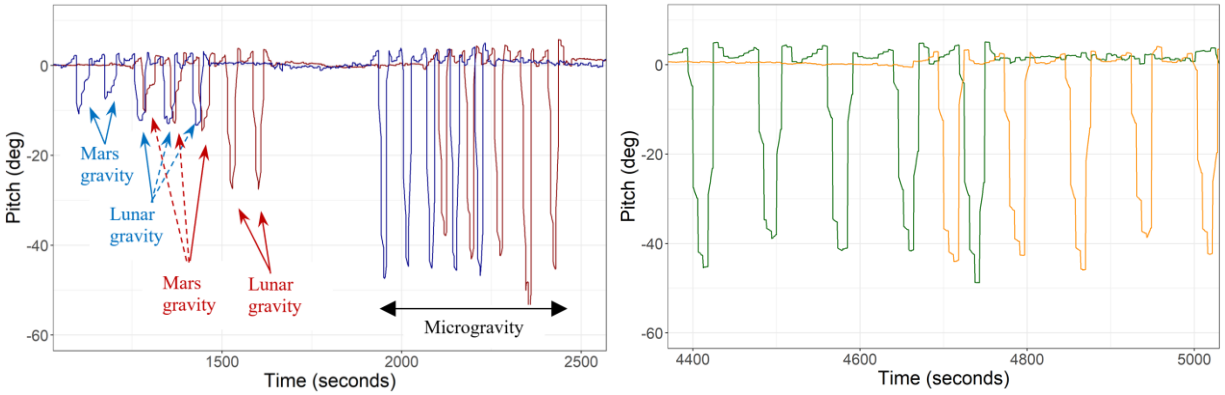

(c) (d)

Fig. 12 Picth angles evolution for some of the parabolas

Fig. 12 shows the relative pitch angle profiles during each of the four flights in the 2020 flight campaign. The first two flights are depicted in Fig. 12a, the last two flights in Fig. 12b. Fig. 12c-d are zoom sections of Fig. 12a-b, respectively, as indicated by the dashed boxes. The pitch angle can also be obtained using a different filter method as in Eq. (10):

$$\theta_{\text{filter}} = \left(\frac{k \cdot \omega \cdot (t - t_0)}{1 - k} + \theta_{\text{accel}} \cdot \frac{180}{\pi}\right) \tag{10}$$

where k is a filter parameter between 0 and 1. A k-value of 0.9 was chosen for all the flights as it preserves the shape of the pitch profile better than values closer to zero. A higher filter parameter is desired since acceleration is more reliable long term. ω is the angular velocity (deg/s) which is the gyro value obtained by the MPU9250 divided by 131. The angular velocity is expressed in 16 bits with ± 250 degrees gyro full rate scale; thus, the least significant bit is $\frac{2^{16}}{500} = 131$. θ_{accel} is the pitch angle based on the acceleration data and can be calculated as in Eq. (11):

$$\theta_{\text{accel}} = \arctan\left(\frac{-a_y}{\sqrt{a_x^2 + a_z^2}}\right) \tag{11}$$

The pitch (filter) profiles for all parabolic flights analyzed is displayed in Fig. 13:

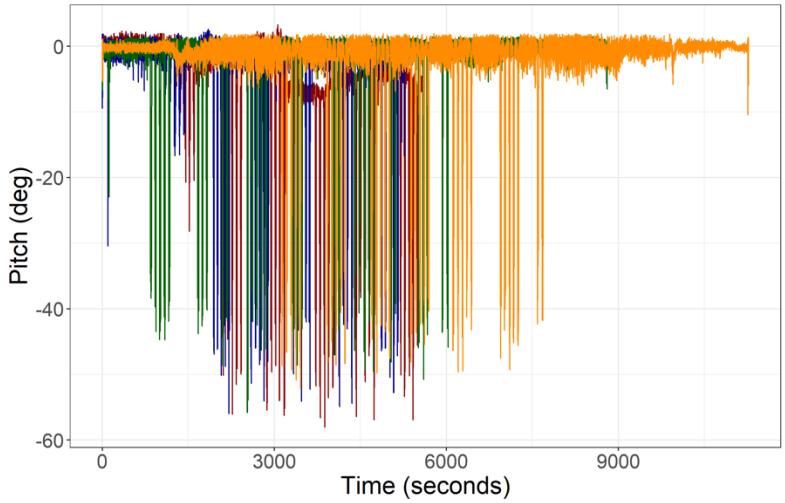

Fig. 13 Picth (filtered) profile evolution for the four flights of the 2020 flight campaign.

C. Velocity Calibration Profiles

We also discuss a calibration method to obtain an approximated velocity profile for the microgravity phases in the Nov 17-18 flights, and for the Nov 19 and 21 flights. In

Fig. **14**, we show only the first 10 parabolas of each of these flights for simplicity.

For the first two flights (sampling rates of 0.383 and 0.385 seconds, respectively), the velocity at time t, V(t) in miles per hour (mph), can be approximated as in Eq. (12):

$$v(t) = \left(\frac{(a(t)+a(t_0))\cdot(t-t_0)}{2} + \frac{a(t_0)\cdot t_0}{66000}\right)\cdot(3600/1.609)\cdot 9.80665\cdot k + k_0 =$$

$$=\left(\frac{a(t)\cdot(t-t_0)}{2} + \frac{a(t_0)\cdot(t-t_0)}{2} + \frac{a(t_0)\cdot t_0}{66000}\right)\cdot(3600/1.609)\cdot 9.80665\cdot k + k_0 =$$

$$=\left(a(t)\cdot\left(\frac{(t-t_0)}{2}\right) + a(t_0)\cdot\left(\frac{(t-t_0)}{2} + \frac{t_0}{66000}\right)\right)\cdot(3600/1.609)\cdot 9.80665\cdot k + k_0 \quad (12)$$

which follows the form: $v(t) = (v(t_0) + a(t)\cdot(t - t_0) + a_{bias}\cdot(t - t_0))\cdot k + k_0$, where k and k_0 are scale factors that vary depending on the sampling rate chosen during data collection (k=18 for first two flights, k=9.5 for last two flights, k_0= 255 for all flights). This bias is not constant but changes over time with both sensor orientation and temperature inside the cabin, which is not constant either as discussed in previous sections. Although this approach may not be optimal, it can be used to decrease the effect of the bias and provide a comparable velocity profile of the aircraft during the weightlessness phase of the parabolic flight (

Fig. **14**). The maximum difference (absolute value) of the sampling rate time vector between the first two flights yielded an error of +0.175 seconds with a standard deviation of 0.039 seconds.

For the last two flights (sampling rates of 0.752 and 0.749 seconds, respectively), the velocity at time t, V(t) can be approximated as the same equation as before but for k = 9.5. The maximum difference (absolute value) of the sampling rate time vector of these two flights was +0.175 seconds and a standard deviation of 0.038 seconds.

The calibrated velocity profiles of the first ten parabolas for each of the four flight campaigns are depicted in Fig. 14 below:

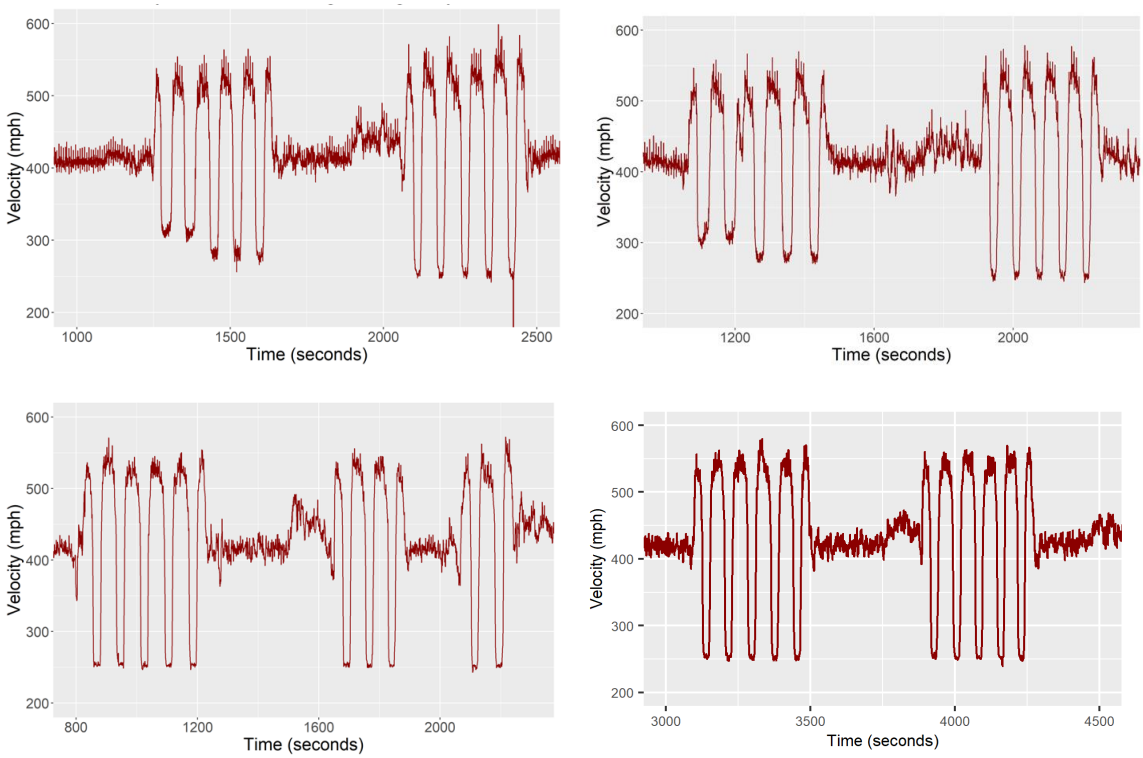

Fig. 14 Velocity profile of the first ten parabolas for each of the four flights of the 2020 flight campaign.

D. Magnetic Field Calibration Profiles

Preliminary calibration of the magnetic field for the X and Y directions can be calculated as in Eq. (13):

$$B_{y,filter} = B_x \cdot \cos(\theta) - B_y \cdot \sin(\theta) \cdot \sin(\psi) + B_z \cdot \sin(\theta) \cdot \cos(\psi)$$

$$B_{x,filter} = B_z \cdot \sin(\theta) + B_y \cdot \cos(\theta) \quad (13)$$

where θ is the pitch angle and ψ is the roll angle. Note that the B_x measured direction corresponds to the real B_z direction (see Fig. **1**).

We compared the magnetic field raw data with the one obtained using the calibrated values Eq. (13) for each flight. We took the average value of over the entire time spectrum and observed a less than one µTesla difference. For the y-component, the error is higher during each parabola where the maximum difference found was 15.0 µTesla and the minimum was 1.E-5 outside the parabola phase. 46.3% of the time, the error is less than 1 µTesla, 22.1% of the time, the error is between 1 and 2 µTesla, 29% of the time, the error is between 2 and 5 µTesla, and 2.6% of the time (parabola phase), the error is between 5 and 14.5 µTesla. As for the x-component, 50% of the time, the time difference was less than 1 µTesla; 17.9% of the time, the error was between 1 and 2 µTesla, during 29.8% of the time, the error was between 2 and 5 µTesla, and during 2.3% of the time, the error was between 5 and 15.5 µTesla (maximum value).

Table 1. Magetic Field Data (Flight vs. Filtered)

Magnetic Field Sensor	Flight Average Measured (µT)	Filtered Average Calculated (µT)	% Flight Time at Condition
Flight #1 Bx (real Bz)	31.3	30.3	<1 µT (50.0%) 1-2 µT (17.9%) 2-5 µT(29.8%) 5-15 µT (2.3%)
Flight #1 By	28.2	27.4	<1 µT (46.3%) 1-2 µT (22.1%) 2-5 µT(29.0%) 5-15 µT (2.6%)
Flight #2 Bx (real Bz)	29.2	27.9	<1 µT (35.8%) 1-2 µT (37.7%) 2-5 µT(24.6%) 5-15 µT (1.9%)
Flight #2 By	24.4	23.4	<1 µT (16.1%) 1-2 µT (46.6%) 2-5 µT(35.3%) 5-15 µT (2.0%)
Flight #3 Bx (real Bz)	38.4	38.7	<1 µT (89.4%) 1-2 µT (5.1%) 2-5 µT(1.4%) 5-20 µT (4.1%)
Flight #3 By	18.0	18.7	<1 µT (91.4%) 1-2 µT (3.4%) 2-5 µT(2.2%) 5-20 µT (3.0%)

Flight #4 Bx (real Bz)	38.5	39.1	<1 μT (74.4%) 1-2 μT (17.9%) 2-5 μT(4.1%) 5-20 μT (3.6%)
Flight #4 By	16.2	17.1	<1 μT (81.4%) 1-2 μT (11.9%) 2-5 μT(3.6%) 5-20 μT (3.1%)

V. Conclusions

The parabolic flight experiment to study the sloshing dynamics of the magneto-active propellant management device experiment was conducted as part of a NASA Flight Opportunities Program aboard the Zero-G aircraft. This research work establishes a benchmark software tool with sloshing analytical formulation and sensor calibration methods that can be used to characterize future research parabolic flights while providing important environmental profiles measured during flight.

VI.Acknowledgments

The authors would like to thank the Applied Aviation Sciences department, Payload Applied Technology & Operations Lab, and Department of Mechanical Engineering at Embry-Riddle Aeronautical University, and Department of Physics and Astronomy at Carthage College. The authors would like to acknowledge the undergraduate and graduate students from both institutions who supported this NASA/Zero-G project. This research was partially supported by the Embry-Riddle Aeronautical University Faculty Research Development Program.

VII. References

[1] Carr, C.E., Bryan, N.C., Saboda, K.N. et al. Acceleration profiles and processing methods for parabolic flight. npj Microgravity 4, 14 (2018). https://www.nature.com/articles/s41526-018-0050-3

[2] Karmali, F., & Shelhamer, M. (2008). The dynamics of parabolic flight: flight characteristics and passenger percepts. *Acta astronautica*, *63*(5-6), 594–602. https://doi.org/10.1016/j.actaastro.2008.04.009

[3] Manikandan Vairamani, Kevin Crosby, Pedro Llanos, Sathya Gangadharan, Somnath Nagendra, "Design and testing of a Field Gradient System to Control a Hybrid Magneto-Active Slosh Control System Using Free Floating Membrane for Cylindrical Propellant Tanks", AIAA SciTech Forum, AIAA-2020-2051, Orlando, January 10, 2020. https://doi.org/10.2514/6.2019-2177

[4] Shelhamer M. (2016). Parabolic flight as a spaceflight analog. *Journal of applied physiology (Bethesda, Md. : 1985)*, *120*(12), 1442–1448. https://doi.org/10.1152/japplphysiol.01046.2015

[5] Friedl-Werner A, Machado M-L, Balestra C, Liegard Y, Philoxene B, Brauns K, Stahn AC, Hitier M and Besnard S (2021) Impaired Attentional Processing During Parabolic Flight. *Front. Physiol*. 12:675426. https://doi.org/10.3389/fphys.2021.675426

[6] Perez-Poch, A., González, D.V., & López, D. (2016). Hypogravity Research and Educational Parabolic Flight Activities Conducted in Barcelona: a new Hub of Innovation in Europe. *Microgravity Science and Technology*, *28*, 603-609

[7] Matthews, K., Motiwala, S., Edberg, D. L. & García-Llama, E. (2012). Flight mechanics experiment onboard NASA's zero gravity aircraft. *Journal of Technology and Science Education* (JOTSE), 2(1), 4-12. http://www.dx.doi.org/10.3926/jotse.26

[8] Llanos, Pedro J., Andrijauskaite, Kristina, Duraisamy, Vijay V., Pastrana, Francisco, Seedhouse, Erik L., Gangadharan, Sathya, Bunegin, Leonid and Rico, Mariel. "Challenges of ERAU's First Suborbital Flight Aboard Blue Origin's New Shepard M7 for the Cell Research Experiment In Microgravity (CRExIM)" *Gravitational and Space Research*, vol.7, no.1, 2019, pp.1-12. https://doi.org/10.2478/gsr-2019-0001

[9] Duraisamy, V.,.Llanos, P., Dikici, B., Crosby, K. & Gangadharan, S. Benchmarking a Multi-Phase Fluid Model of a Slosh Mitigation Device in Microgravity Utilizing Parabolic Flight Test Data. International Mechanical Engineering Congress and Exposition, November 2022, IMECE2022-99385.

[10] Sesha, N.C. Govindan, & Michael E. Dreyer (2018). Experimental Investigation of Liquid Interface Stability During the Filling of a Tank in Microgravity. Microgravity Science and Technology (2023) 35:23 https://doi.org/10.1007/s12217-023-10044-1

[11] P. A. Caron, M. A. Cruchaga, A. E. Larreteguy; Study of 3D sloshing in a vertical cylindrical tank. *Physics of Fluids* 1 August 2018; 30 (8): 082112. https://doi.org/10.1063/1.5043366
[12] Pengxiang, Hu, Zhihua Zhao, Shutao Yang, Yaoxiang Zeng, and Feng Qi. Study on Equivalent Sloshing Mass Locations for Liquid-Filled Cylindrical Tanks. American Institute of Aeronautics and Astronautics, September 2021. https://doi.org/10.2514/1.A35098
[13] Daogang Lu, Xiaojia Zeng, Junjie Dang, and Yu Liu. A Calculation Method for the Sloshing Impact Pressure Imposed on the Roof of a Passive Water Storage Tank of AP1000. Hindawi Publishing Corporation, Science and Technology of Nuclear Installations, Volume 2016, Article ID 1613989, 8 pages. http://dx.doi.org/10.1155/2016/1613989
[14] Crosby, Kevin M., Werlink, Rudy J. and Hurlbert, Eric A. "Liquid Propellant Mass Measurement in Microgravity" Gravitational and Space Research, vol.9, no.1, 2021, pp.50-61. https://doi.org/10.2478/gsr-2021-0004
[15] Christian Meyer, Overview of TVOC and Indoor Air Quality (White paper), Renesas Electronics Corporation, https://www.renesas.com/us/en/document/whp/overview-tvoc-and-indoor-air-quality